12-1-2014

Spatial and Seasonal Variations in Aridification Across Southwest North America

Shannon Miller Jones

Follow this and additional works at: https://digitalrepository.unm.edu/eps_etds

Shannon M. Jones
Candidate

Earth and Planetary Sciences
Department

This thesis is approved, and it is acceptable in quality and form for publication:

Approved by the Thesis Committee:

David S. Gutzler, Chair

Peter J. Fawcett

Joseph Galewsky

SPATIAL AND SEASONAL VARIATIONS IN ARIDIFICATION ACROSS SOUTHWEST NORTH AMERICA

BY

SHANNON M. JONES

B.S., ENVIRONMENTAL SCIENCE, UNIVERSITY OF NEW MEXICO, 2008

THESIS

Submitted in Partial Fulfillment of the
Requirements for the Degree of

Master of Science

Earth and Planetary Science

The University of New Mexico
Albuquerque, New Mexico

December 2014

ACKNOWLEDGEMENTS

SPATIAL AND SEASONAL VARIATIONS IN ARIDIFICATION ACROSS SOUTHWEST NORTH AMERICA

by

Shannon M. Jones

B.S., Environmental Science, University of New Mexico, 2008
M.S., Earth and Planetary Science, University of New Mexico, 2014

ABSTRACT

The Southwestern region of North America (SWNA) is projected to become more arid throughout the 21st century as precipitation (P) and evaporation (E) rates change with increasing global temperatures. Trends in the regional surface moisture balance (P–E) of SWNA vary between the arid southern subregion (mostly Northern Mexico) and the more temperate northern subregion (Southwest US), depending on the relative contributions of cold and warm season P and E. Interpreting the spatial and seasonal variations of the projected aridification is important for understanding the potential impacts of climate change on SWNA regional hydrology.

We compare the projected trends in P, E, and P–E in CMIP5 global climate model projections, for the northern and southern subregions of SWNA between the extended cold and warm seasons. Both subregions become drier (i.e., negative trend in P–E) in the 21st century. The drying trend is biggest in the cold season surface moisture balance, which contributes much of the base flow to rivers in the Southwest US. We show that the downward trend in the cold

season P–E is caused primarily by increasing E in the northern subregion, and by decreasing P in the southern subregion. Decreasing P is the primary contributor to small warm season drying trends in the northern and southern subregions of SWNA.

P accounts for most of the interannual variability in SWNA P–E and is strongly correlated with Pacific Ocean temperature anomalies associated with the El Niño Southern Oscillation and the Pacific Decadal Oscillation during the cold season. However, SWNA aridification is distinguished from the region's natural climate variability because it is caused by long-term trends in P and E that are related to global warming. This is most evident in the cold season surface moisture balance of the northern subregion, where the temperature-driven trend in E (upward) is greater than the trend in P (downward). Trends in P and E account for a considerable fraction of the total variance in 21st century P–E and cause the cold season surface moisture balance of the northern and southern subregions to drop below the range of interannual variability by the end of the 21st century.

TABLE OF CONTENTS

LIST OF FIGURES

LIST OF TABLES

Chapter 1

Introduction

Drought, defined as a precipitation deficit below the climatological average, is a normal part of the natural climate variability of Southwestern North America (SWNA) [Woodhouse et al. (2010)]. SWNA precipitation fluctuates on multidecadal time scales and is modulated by remote sea surface temperature anomalies associated with the El Niño Southern Oscillation (ENSO), the Pacific Decadal Oscillation (PDO), and the Atlantic Multidecadal Oscillation (AMO) [Ropelewski and Halpert (1986); McCabe et al. (2004); Schubert et al. (2009)]. The droughts of the 1930s, 1950s, and early 2000s are examples of how persistent dry conditions can affect the regional hydrology, ecosystems, and economies across SWNA.

Anthropogenic global warming has induced observed and simulated changes in western hydrology, including parts of SWNA, since the latter half of the 20th century [Barnett et al. (2008); Cayan et al. (2010)]. Some of the hottest and driest years on record for SWNA occurred during the early 21st century, even though precipitation remained within the range of natural variability [Barnett et al. (2008)]. Climate model projections indicate that dry conditions throughout SWNA will worsen over the next century as a function of long-term trends in precipitation (P) and evaporation (E) [Seager et al. (2007); Hoerling and Eischeid (2007); Gutzler and Robbins (2010)]. However, unlike the episodic ocean-forced precipitation deficits that characterize historical SWNA drought, the projected 21st

century aridification is instead a transition to sustained drier conditions that will inhibit drought recovery in the future [Gutzler and Robbins (2010)]. SWNA aridification is consistent with the observed and simulated global trends towards wet regions getting wetter and dry regions getting drier [Held and Soden (2006); IPCC (2013)] as well as the poleward shift of the Hadley circulation and expansion of the subtropical dry zone as the climate warms [Yin (2005); Seidel et al. (2008)].

Hydroclimate varies both spatially and seasonally across SWNA, depending on the relative contributions of warm and cold season P. The contribution of cold season P to the annual total is large for the northern (Southwestern US) half of SWNA, where the headwaters of many Southwestern US rivers originate and are fed by snowmelt runoff. The warm season P contribution is higher in the southern (mostly Northern Mexico) half of SWNA, where the North American Monsoon is centered [Douglas et al. (1993)]. Projections from the third Coupled Model Intercomparison Project (CMIP3) archive indicate that an annually averaged downward trend in the 21st century surface moisture balance ($P - E$) is caused by an average decrease in P over a large area of SWNA, including both the northern and southern subregions alluded to above [Seager et al. (2007)]. However, Gutzler and Robbins (2010) show the drying trend in CMIP3 projections for NM Climate Division 2 (within the northern half of the Seager et al. (2007) averaging region) is caused by a

temperature-driven increase in E, while the projected trend in P is statistically indistinguishable from zero.

The purpose of the present analysis is to interpret the spatial and seasonal aspects of SWNA aridification. Understanding how P and E contribute to 21st century aridification at different times of the year is important for water management and regional development because regional water demands and availability vary across SWNA and change throughout the year. We analyze the trends and interannual variability in P, E, and $P - E$ using 18 models from the CMIP5 archive. SWNA is divided into northern and southern subregions, as defined in Section 2, and the relative roles of P and E are compared between the warm and cold seasons in order to diagnose the causes of SWNA aridification.

In Section 3 we show that long-term trends in P (downward) and E (upward) both contribute to a downward trend in $P - E$ that is robust in CMIP5 projections for SWNA. We find that an annually averaged downward trend in $P - E$ across the entire SWNA region is caused by decreasing P in CMIP5 simulations, which is consistent with what Seager et al. (2007) showed using CMIP3 simulations. However, by parsing the trends in P, E, and $P - E$ by season and subregion, we show important spatial and seasonal differences in SWNA aridification. Cold season $P - E$ drops below the range of interannual variability by the end of the 21st century as a function of increasing E in the northern subregion, and decreasing P in the southern subregion. Warm season

aridification is caused by a decrease in P across SWNA, but remains within the range of interannual variability throughout the 21st century.

In Section 4 we put trends into the context of interannual variability. We analyze the correlations between SWNA P (which accounts for most of the interannual variability in $P - E$) and remote ocean surface air temperature anomalies to see whether the CMIP5 models simulate the observed oceanic climate variability indices that modulate interannual variability in SWNA P. We find that much of the simulated interannual variability in SWNA P is correlated with temperature anomalies associated with ENSO and PDO during the cold season, especially in the northern subregion of SWNA. The role of the trend in modulating the total variance in cold season $P - E$ increases throughout the 21st century as the impacts of anthropogenic global warming become more pronounced in the seasonal surface moisture balance across SWNA.

Chapter 2

Models and Methods

Trends and variability in precipitation (P), evaporation (E), and the net vertical flux of water into the surface $(P - E)$ are analyzed using an ensemble of 18 climate models (Table 1) from the fifth Coupled Model Intercomparison Project (CMIP5) archive [Taylor et al. (2012)]. All simulations considered are generated from the CMIP5 Historical and Representative Concentration Pathway 8.5 (RCP8.5) experiments [Moss et al. (2010)], using a single iteration per model. Model simulations from the Historical period (1861-2005) are forced with estimated solar irradiance, natural and anthropogenic aerosols, and historical greenhouse gas concentration. Simulations from the RCP8.5 period (2006-2100) use prescribed future solar irradiance and aerosols, and greenhouse gas concentration derived from an emissions pathway that increases the anthropogenic radiative forcing by 8.5 W/m^2 relative to preindustrial conditions by the year 2100 [Moss et al. (2010); Meinshausen et al. (2011), IPCC (2013)]. RCP8.5 introduces the largest future radiative forcing out of all of the RCP emissions scenarios used in the Intergovernmental Panel on Climate Change Fifth Assessment Report (IPCC AR5) [Moss et al. (2010); Meinshausen et al. (2011), IPCC (2013)].

Model output includes P (CMIP5 variable pr) and latent heat flux (CMIP5 variable hfls) values in monthly-averaged increments. The latent heat flux is

5

converted to a water flux (evaporation, E) using a constant value for the latent heat of vaporization ($2.5 \times 10^6 \mathrm{Jkg}^{-1}$). Values of P and E are converted to units of mm/month. We calculate the net vertical flux of water into the ground surface as the difference P minus E. This difference approximates a surface moisture balance, to the extent that the horizontal and subsurface vertical moisture fluxes are negligible when calculating monthly $\mathrm{P} - \mathrm{E}$ at the top of a three-dimensional box extending downward from the ground surface. The surface moisture balance can also be approximated as the difference between moisture convergence and divergence within a column of air extending upward from the ground surface [Seager et al. (2007)]. Calculating $\mathrm{P} - \mathrm{E}$ directly from the surface moisture fluxes P and E allows us to differentiate the cause of trends in $\mathrm{P} - \mathrm{E}$ and to interpret important seasonal differences between warm and cold season aridification across the climatically variable landscape of SWNA.

This paper defines the region of SWNA as the land surface area ranging from 25°N to 40°N and 99°W to 117°W, which includes most of the Southwest US and Northern Mexico. This area shares the same northern and southern boundaries as the region considered by Seager et al. (2007). For this study, SWNA is divided into northern and southern subregions at latitude 32.5°N, near the US-Mexico border (Figure 1a). The northern subregion (hereafter SWNA$_\mathrm{N}$) encompasses the more temperate areas of the Southwest US where cold season P, much of which falls as snow, accounts for >50% of the annual total in the northern and western parts of the subregion [Climatology-6 Month (2014)]. The

southern subregion (hereafter SWNA$_S$) encompasses the more arid parts of SWNA, including Northern Mexico, where warm season precipitation, much of which falls during the monsoon season, accounts for >60% to >80% of the annual total in the southern and eastern parts of the subregion [Climatology-6 Month (2014); Douglas et al. (1993)].

For each model, the monthly values of P and E are averaged spatially across SWNA$_N$, SWNA$_S$, and the combined northern and southern subregions (denoted SWNA without a subscript) by calculating the mean of the whole grid cells located completely within or <1° outside the boundaries of the averaging regions. For a model with 1.25° by 1.875° resolution, this equates to approximately 93 grid cells averaged over the entire SWNA. Output from grid cells containing ≥20% ocean surface are not included in the spatial averages. Time series of the spatially averaged seasonal P and E are produced for SWNA$_N$, SWNA$_S$, and SWNA by calculating the mean of the monthly spatial P and E averages over every cold (December-May) and warm (June-November) half-yearly season from 1861-2100. The resulting time series is a single annual value of P and E for the cold season (^{C}SWNA$_N$, ^{C}SWNA$_S$, and ^{C}SWNA) and the warm season (^{W}SWNA$_N$, ^{W}SWNA$_S$, and ^{W}SWNA), for each model.

Time series of the spatially averaged seasonal P and E from the Historical and RCP8.5 periods are concatenated to form continuous time series (1861-2100) for each model. The 1861-2100 time series of P, E, and $P - E$ for each of the 18 models plus the ensemble mean are shown for the northern subregion

during the cold season (Figure 2). Time-mean P and E are calculated for the initial century (1861-1960) to estimate the simulated historical average before atmospheric CO_2 concentration and global temperatures began to increase rapidly in the late 20th century. The 1861-1960 mean P and mean E values are subtracted from the 1861-2100 time series. This procedure facilitates comparison between model simulations by removing systematic model biases determined from the 1861-1960 historical period. Hereafter we refer to the 1861-2100 spatially averaged seasonal P and E time series with model biases removed as the normalized time series.

The normalized P and E time series are used to calculate $P - E$ for each model as well as annual values of the 18-model ensemble mean precipitation ($\overline{P}$), mean evaporation ($\overline{E}$), mean surface moisture balance ($\overline{P - E}$), and the entire 18-model ensemble $(P - E)'$ interquartile range (25th to 75th percentiles), for the two half-yearly seasons and each averaging region.

8

Chapter 3

Historical and Projected Trends in P, E, and P–E

Ensemble mean time series (1861-2100) of $\overline{P}$ (blue line), $\overline{E}$ (red line) and $\overline{P-E}$ (green line) are plotted for $^{C}SWNA_{N}$, $^{C}SWNA_{S}$, $^{W}SWNA_{N}$, and $^{W}SWNA_{S}$ (Figure 4). Deviations of $\overline{P}$, $\overline{E}$, and $\overline{P-E}$ from y=0 (black line) reflect the ensemble mean interannual variability relative to the 1861-1960 simulated historical average. The interquartile range of $(P-E)'$, which illustrates the inter-model variability of the ensemble, is shown as a smoothed envelope using a 21-year centered moving average (gray shading). The fraction of total variance in the 1861-2100 $\overline{P-E}$ that is accounted for by $\overline{P}$ is shown for each subregion and season.

Interannual fluctuations in $\overline{P-E}$ occur throughout the 1861-2100 time series with an overall decrease in $\overline{P-E}$ across SWNA in both the warm and cold seasons. The biggest decrease in $\overline{P-E}$ occurs during the 21st century (RCP8.5) portion of each time series. The downward trend in $\overline{P-E}$ is especially pronounced in $^{C}SWNA_{S}$, where $\overline{P}$ decreases faster than $\overline{E}$ (Fig. 4c). In $^{C}SWNA_{N}$, increasing $\overline{E}$ causes the downward trend in $\overline{P-E}$, while there is little trend in $\overline{P}$ (Fig. 4a). There are smaller but notable downward warm season trends in $\overline{P-E}$ for both $^{W}SWNA_{N}$ and $^{W}SWNA_{S}$, where $\overline{P}$ decreases faster than $\overline{E}$ (Fig. 4b,d). $\overline{P}$ accounts for most (≥51%) of the total interannual variance in $\overline{P-E}$, while the

fraction of variance accounted for by $\bar{E}$ (not shown) is smaller than $\bar{P}$ for each subregion and season.

Secular trends in $\bar{P}$, $\bar{E}$, and $\overline{P-E}$ are quantified via linear regression (Table 2). Gutzler and Robbins (2010) showed that linearity is a good assumption for CMIP3 projections of temperature and P using a different emissions scenario and set of CMIP3 simulations. Trend significance is assessed against a null hypothesis of zero using a two-tailed t-test at the 5% significance level. The downward trend in annually averaged $\overline{P-E}$ across the entire SWNA (denoted [A]SWNA) is primarily caused by a downward trend in $\bar{P}$, which is consistent with a conclusion of Seager et al. (2007) based on CMIP3 simulations.

However, by parsing the effects of $\bar{P}$ and $\bar{E}$ by subregion and season, we find that the cause of the drying trend in $\overline{P-E}$ is not uniform across SWNA throughout the year. SWNA aridification is most pronounced in the cold season surface moisture balance equations for both [C]SWNA$_N$ and [C]SWNA$_S$. The biggest downward trend in $\overline{P-E}$ occurs in [C]SWNA$_S$ and is caused by a decrease in $\bar{P}$, while $\bar{E}$ decreases over time. The drying trend for [C]SWNA$_N$ is primarily caused by an increase in $\bar{E}$, while there is a small but statistically insignificant decrease in $\bar{P}$. Warm season drying in [W]SWNA$_N$ and [W]SWNA$_S$ is caused by downward trends in $\bar{P}$, while $\bar{E}$ decreases over time.

Next we compare the projected $\overline{P-E}$ time series to a future without the RCP8.5-associated trends. The linear trend in $\overline{P-E}$ is calculated over the projected (RCP8.5, 2006-2100) portion of the normalized time series for

^{C}SWNA$_N$, ^{C}SWNA$_S$, ^{W}SWNA$_N$, and ^{W}SWNA$_S$ (Figure 5). The linear trend (black line) is subtracted from the 2006-2100 normalized $\overline{P-E}$ time series (hereafter, projected $\overline{P-E}$; red line) in order to calculate a detrended 2006-2100 time series (hereafter detrended $\overline{P-E}$; blue line) and range of interannual variability (blue shading) for each subregion and season. The fraction of total interannual variance in each of the projected $\overline{P-E}$ time series that is accounted for by the linear trend is shown.

21st century aridification is most pronounced in the cold season, when the projected $\overline{P-E}$ for both ^{C}SWNA$_N$ and ^{C}SWNA$_S$ consistently drops below the simulated historical average (y=0) (Fig. 5a,c). The range of interannual variability in cold season $\overline{P-E}$ is largest in ^{C}SWNA$_N$ (during the primary precipitation season of SWNA$_N$) (Fig. 5a,c). Cold season downward trends in $\overline{P-E}$ are big compared to the range of interannual variability and account for a considerable fraction (28% in ^{C}SWNA$_S$ and 18% in ^{C}SWNA$_N$) of the total interannual variance in cold season $\overline{P-E}$.

The biggest difference between the projected and detrended $\overline{P-E}$ time series occurs in ^{C}SWNA$_S$, where the downward trend in $\overline{P-E}$ is large and the range of interannual variability is relatively small. ^{C}SWNA$_S$ $\overline{P-E}$ begins to drop below the range of interannual variability around midcentury and lies completely outside of it by 2100 (Fig. 5c). The projected cold season $\overline{P-E}$ for ^{C}SWNA$_N$ stays within the relatively large range of interannual variability until about 2090 (Fig. 5a). However, wet anomalies (when projected $\overline{P-E} > 0$) become less frequent

throughout the 21st century, indicating that the downward trend in ^{C}SWNA$_N$ $\overline{P-E}$ starts to inhibit drought recovery before 2090.

Changes in aridity are smaller in the warm season surface moisture balances of SWNA$_N$ and SWNA$_S$. With the exception of a few anomalously dry years, warm season $\overline{P-E}$ for both ^{W}SWNA$_N$ and ^{W}SWNA$_S$ stays within the range of interannual variability throughout the 21st century (Fig. 5b,d). The ranges of interannual variability in warm season $\overline{P-E}$ are similar to the cold season ranges for ^{C}SWNA$_N$ and ^{C}SWNA$_S$, except the range is bigger for ^{W}SWNA$_S$ (primary precipitation season in SWNA$_S$) than for ^{W}SWNA$_N$ (Fig. 5b,d). However, warm season trends in $\overline{P-E}$, which account for only 1.1% of the total interannual variance in warm season $\overline{P-E}$, are much smaller than cold season trends. This makes a big difference in determining how much the projected seasonal surface moisture balance changes relative to the natural interannual variability of SWNA climate.

Chapter 4

Interannual Variability of the Surface Moisture Balance

To explore the mechanisms that generate SWNA interannual variability within the CMIP5 simulations, we analyze the correlations between SWNA P and ocean surface air temperature anomalies (T, CMIP5 variable tas) in regions associated with the Atlantic Multidecadal Oscillation (AMO), the Pacific Decadal Oscillation (PDO) and the El Niño Southern Oscillation (ENSO). Monthly values of T are averaged spatially across the North Atlantic (NAtl; 5°N-60°N, 52°W-17°W), North Pacific (NPac; 21°N-49°N, 186°W-138°W), and Tropical Pacific (TPac; 5°S-5°N, 170°W-120°W) oceans to reproduce the influence of the AMO, PDO, and ENSO climate variability indices (Fig. 1b).

Detrended P time series are calculated for ^{C}SWNA$_N$, ^{C}SWNA$_S$, ^{W}SWNA$_N$, and ^{W}SWNA$_S$ by removing the trend from the unprocessed (not normalized) Historical and RCP8.5 P time series for each model. The individual model monthly NAtl, NPac, and TPac T time series are averaged over every cold (^{C}NAtl, ^{C}NPac, and ^{C}TPac) and warm (^{W}NAtl, ^{W}NPac, and ^{W}TPac) season within the Historical and RCP8.5 periods for each model. Cold season TPac T time series (1861-2100) for each model plus the ensemble mean show the spread of the 18-model output (Figure 3). Cold season TPac T increases rapidly beginning in the year 2006 when the anthropogenic radiative forcing starts to follow the RCP8.5 emissions pathway. Trends in T are subtracted from the time series to remove

13

the influence of the trend from the total variance. Hereafter we refer to the spatially averaged seasonal ocean surface air temperatures with trends removed as the detrended T time series.

Correlations between the detrended T and detrended P time series for each subregion and season are calculated for each of the 18 models. The correlations between TPac T and NPac T, as well as the lag correlations between ^{C}TPac T and the following warm season ^{W}SWNA P, and between ^{C}TPac T and the following warm season ^{W}TPac T are calculated to explore the extent to which observed aspects of the ENSO and PDO indices and their influence on climate variability in SWNA are simulated in the models [Ropelewski and Halpert (1986); Gutzler and Preston (1997), Gutzler et al. (2002)].

Correlations are considered significant if the null hypothesis of zero is rejected at α = 0.05 and if the correlation coefficient agrees in sign with observation-based results: r>0 for r(SWNA P, TPac T), and r<0 for r(SWNA P, NPac T), r(SWNA P, NAtl T), and r(TPac T, NPac T) [McCabe et al. (2004); Ropelewski and Halpert (1986); Gershunov and Barnett (1998)]. Due to uncertainty about whether the expected signs of the lag correlations, r(^{C}TPac T, ^{W}SWNA P) and r(^{C}TPac T, ^{W}TPac T), are positive or negative in the literature [Gutzler and Preston (1997)], we consider these correlations to be significant if the null hypothesis of zero is rejected at α = 0.05, regardless of the sign of r.

The percentage of the 18 CMIP5 simulations that yield significant correlations between SWNA P and T in the NAtl, NPac, and TPac is shown for

the Historical and RCP8.5 periods for each subregion and season (Table 3). Cells in which the percentage is greater than 33% are highlighted in orange where the expected sign of the correlation is r<0, and in blue where r>0. The percentage of simulations that yield significant correlations for r(TPac T, NPac T) and for the lag correlations r(^{C}TPac T, ^{W}SWNA P) and r(^{C}TPac T, ^{W}TPac T) are not shown in Table 3 but are discussed below.

The CMIP5 models show a strong (≥50%) tendency to simulate the ENSO-associated correlation between TPac T and SWNA P in the warm and cold seasons (Table 3a-d). The number of models that simulate r(TPac T, SWNA P) is higher in the cold season, which is consistent with the observation that ENSO primarily effects P in the Southwest US during the winter [Gutzler et al. (2002); Llewellyn et al. (2103)]. This is especially true for ^{C}SWNA$_N$ (Table 3a) where the percentage of models that simulate the cold season ENSO correlation is 94% for the Historical period and 89% for the RCP8.5 period. The ENSO correlation tends to weaken in the future RCP8.5 period, especially in ^{C}SWNA$_S$ (Table 3c). Fewer (≤28%) models simulate a significant lag correlation between ^{C}TPac T and the following ^{W}SWNA P in either subregion (not shown).

The models show a weaker, but still significant, tendency to simulate the cold season PDO-associated correlation between NPac T and SWNA P in ^{C}SWNA$_N$ (≥61% for the Historical and RCP8.5 simulations; Table 3a) and in ^{C}SWNA$_S$ (39% for the Historical simulation only; Table 3c). Comparing results in Table 3a, we see that CMIP5 simulations are consistent with the observation-

15

based results by Gutzler et al. (2002) that ENSO plays a primary role in modulating cold season P in the Southwest US ($SWNA_N$ subregion), while PDO plays a secondary role. The tendency for the models to simulate the PDO correlation during the warm season is very weak (≤ 6%) in both subregions. CMIP5 models show a very weak (0-17%) tendency to simulate the AMO-associated correlation between NAtl T and SWNA P in each subregion and season.

The models show a strong tendency (≥72%) to simulate the observed negative correlation between TPac T and NPac T during the cold season in the Historical and RCP8.5 simulations. This tendency is much weaker (≤17%) during the warm season. The percentage of models that simulate the correlation between ^{C}TPac T and the following warm season ^{W}TPac T is 83% for the Historical period and 61% for the RCP8.5 period.

In Section 3 we showed that most of the total interannual variance in $\overline{P - E}$ is accounted for by $\overline{P}$ in CMIP5 simulations of climate from 1861-2100. Here, we show that much of the interannual variability in SWNA $\overline{P}$ is related to Pacific Ocean surface air temperature anomalies associated with ENSO and PDO. The ENSO and PDO signals are strongest in $^{C}SWNA_N \overline{P}$, which is consistent with observations. We find that cold season Pacific Ocean surface air temperature anomalies associated with ENSO and PDO are significantly correlated, which is also consistent with observations. CMIP5 models therefore show skill in realistically simulating the ENSO and PDO climate variability indices that

16

modulate SWNA $\overline{P-E}$ variability, which justifies the comparison between long-term trends and interannual variability in SWNA $\overline{P-E}$ for distinguishing SWNA aridification from the episodic ocean-forced precipitation deficits that characterize historical drought.

Chapter 5

Discussion

We have shown that an ensemble of 18 CMIP5 climate models project a transition to a sustained drier climate, defined in terms of $P - E$, across SWNA over the next century. Distinguishing the cause and magnitude of aridification between the northern and southern subregions of SWNA and between the warm and cold half-yearly seasons is important for understanding the potential impacts of climate change on SWNA regional hydrology. SWNA aridification is most pronounced in the cold season surface moisture balance, which strongly affects Southwestern US rivers, and therefore has important implications for water management, ecology, and the regional economy [Williams et al. (2010); Hurd and Coonrod (2012); Llewellyn et al. (2013)].

Cold season aridification in $SWNA_N$ (US portion), where much of the Southwestern US river base flows originate as snowpack, is caused by a temperature-driven increase in $\overline{E}$ while the downward trend in $\overline{P}$ is statistically indistinguishable from zero. The transition from cold season snow to rain in $SWNA_N$ further promotes $\overline{E}$ as global temperatures increase [Mote (2003); Knowles et al. (2006)]. Sustained drying occurs in $^CSWNA_N$ throughout the 21st century, with $\overline{P - E}$ eventually falling below the range of historical interannual variability. Comparing the r^2 values in Figure 4 and the linear trend coefficients in Table 2, we conclude that the role of $\overline{E}$ in modulating $\overline{P - E}$ variability is small for

18

interannual fluctuations, but accounts for a large fraction of century-scale drying in ^{C}SWNA$_N$. By diagnosing the downward trend in ^{C}SWNA$_N$ $\overline{P-E}$ as a function of a long-term trend in E, we have shown that 21st century aridification of ^{C}SWNA$_N$ differs from the more episodic, ocean-forced precipitation deficit droughts of the past.

The biggest increase in aridity occurs in ^{C}SWNA$_S$ (mostly Northern Mexico) during the cold season and is caused by a big downward trend in $\overline{P}$. This result reproduces IPCC AR5 (2013), which shows a big decrease in P across Northern Mexico. Increased aridity in ^{C}SWNA$_S$, which is caused by a downward trend in ^{C}SWNA$_S$ $\overline{P}$, is partially compensated by a downward trend in $\overline{E}$ as the amount of surface moisture available for evaporation decreases. Ocean-forced interannual fluctuations in SWNA $\overline{P}$ are superimposed onto a downward trend in cold season $\overline{P-E}$. The role of $\overline{P}$ in modulating $\overline{P-E}$ interannual variability is large over the period 1861-2100, however the role of the trend in $\overline{P-E}$ becomes increasingly important during the 21st century, contributing 28% of the total interannual variance in ^{C}SWNA$_S$ $\overline{P-E}$ over the century. The downward trend in cold season $\overline{P}$, which occurs in SWNA$_S$ but not in SWNA$_N$, signals a northward shift of the winter storm track and supports the hypothesis that the upper branch of the Hadley circulation expands poleward in a warmer climate, leaving northern Mexico hanging out to dry in the cold season.

Warm season aridification in SWNA$_N$ and SWNA$_S$ is caused by a decrease in $\overline{P}$, while $\overline{E}$ also decreases as the surface dries out. The decrease in warm

season $\overline{E}$ is expected to amplify warm season surface warming across SWNA [Cayan et al. (2010); IPCC (2013); Melillo et al. (2014)]. Warm season aridification, coupled with elevated temperatures, will impact agricultural and ecological water demands as well as the occurrence of heat waves and wildfires throughout the region [Westerling et al. (2006); Williams et al. (2010); Gutzler (2013); Melillo et al. (2014)]. In both SWNA$_N$ and SWNA$_S$, downward trends in $\overline{P-E}$ are smaller in the warm season and remain within the envelope of interannual variability throughout the Historical and RCP8.5 periods. The trend accounts for ≤1.1% of the total interannual variance in 21st century warm season $\overline{P-E}$, indicating that $\overline{P}$ will continue to play a primary role in modulating interannual fluctuations of warm season $\overline{P-E}$ over the next century.

The CMIP5 models reproduce the observed interannual correlations between SWNA $\overline{P}$ and ocean surface air temperature anomalies associated with ENSO and PDO. This relationship is strongest in ^{C}SWNA$_N$ where the winter storm track contributes a large fraction of annual P, but weakens in ^{C}SWNA$_S$ where the cold season P contribution is smaller. Consistent with the observation that ENSO is the leading mode of interannual variability in cold season SWNA P, we find that the models most frequently reproduce correlations associated with ENSO. The models also show skill in simulating the observed negative correlation between cold season T anomalies associated with ENSO and PDO [Gershunov and Barnett (1998); Mantua and Hare (2002)]. Correlations associated with SWNA P and the ENSO and PDO indices weaken in the warm

season, as much of the warm season P in SWNA is generated via localized moist convection rather than large-scale dynamics that are influenced by ocean temperature anomalies.

For both averaging regions and seasons, $\overline{P}$ accounts for a larger fraction than $\overline{E}$ of the total variance in 1861-2100 $\overline{P-E}$. Comparing the results in Figure 4 and Table 3, we conclude that ENSO and PDO dynamics, which are internal to the models, generate much of the total interannual variance in cold season $\overline{P-E}$ time series for $SWNA_N$ and $SWNA_S$, especially during the Historical (1861-2005) period. The tendency for the models to simulate the ENSO-associated cold season correlation between TPac T and SWNA P weakens in the 21st century (RCP8.5) simulations, especially in $^CSWNA_S$. The weaker statistical coupling is consistent with the increasing importance of the $\overline{P}$-driven downward trend in $\overline{P-E}$, whose relative contribution to the total interannual variance in $\overline{P-E}$ increases throughout the 21st century as the winter storm track moves north in a warmer climate.

It is important to acknowledge the uncertainty that is inherent in the use of general circulation models (GCMs) to study the climate system. Many studies have compared GCM output with observations and conclude that the models are skillful at simulating climate patterns that are generated via large-scale dynamics [IPCC (2013)]. The projected increase in global temperatures that is robust among the CMIP5 models is one example of this [IPCC (2013)]. The long-term changes in the position of the winter storm track that we see evidence for in the

CMIP5 simulations is another example. There is more uncertainty in climate patterns that are generated via sub-grid scale processes, such as warm season thunderstorms generated via moist convection, which tend to be more stochastic than those that are generated via large-scale dynamical processes [Cook and Seager (2013)]. This may explain why the trends in warm season $\overline{P-E}$ remain small compared to 21st century interannual variability, as compared to the cold season.

Output can vary widely among the models, depending on the model resolution, interaction between model components, parameterizations, and other factors. Precipitation simulations tend to differ significantly from one model to the next [Zhang et al. (2007); IPCC (2013)]. We have calculated the mean $\overline{P}$, $\overline{E}$, and $\overline{P-E}$ using 18 climate models to represent our best indication of future conditions while providing information about the range of uncertainty within the ensemble. By doing so, we assume that the models show equal skill in simulating SWNA P, E, and $P-E$. Much of the individual model variance is averaged out of the ensemble mean, however we retain the inter-model variations by showing the smoothed interquartile range of $(P-E)'$ in Figure 4.

The use of the RCP8.5 emissions scenario introduces uncertainty related to future socioeconomic conditions, technology, public policy, and other factors. The RCP8.5 emissions scenario introduces the largest anthropogenic radiative forcing out of all of the RCP scenarios. We use model output from the RCP8.5 experiments to show the higher-end projected changes in P, E, and $P-E$, but

22

acknowledge that the actual future anthropogenic radiative forcing may deviate significantly from the RCP8.5 trajectory, depending on a variety of social and environmental factors.

Chapter 6

Summary and Conclusions

We examine SWNA aridification over the period 1861-2100 by comparing warm and cold season trends and interannual variability in P, E, and $P-E$ between the northern, southern and combined subregions of SWNA using 18 model simulations from the CMIP5 archive. Using this approach, we show that the cause and magnitude of SWNA aridification varies between the warm and cold seasons across the largely defined region of SWNA. We compare the projected (2006-2100) $\overline{P-E}$ time series to a future without the RCP8.5-associated trends to see how century scale trends affect 21st century $\overline{P-E}$ relative to the interannual variations that are a normal feature of SWNA climate. We calculate the correlations between seasonal SWNA P and remote ocean surface air temperature anomalies associated with ENSO, PDO, and AMO to infer the mechanisms that generate interannual variability within the CMIP5 models.

We show that SWNA aridification is a robust feature in CMIP5 projections of 21st century $\overline{P-E}$ for the warm and cold half-yearly seasons. This result is consistent with previous analyses of CMIP3 projections [Seager et al. (2007); Hoerling and Eischeid (2007); Gutzler and Robbins (2010)] and the hypothesis that dry areas become drier in a warmer climate regime [Held and Soden (2006); IPCC (2013)]. CMIP5 projections are consistent with the Seager et al. (2007)

conclusion that the annually averaged drying trend in $\overline{P - E}$ across the largely defined SWNA (SWNA$_N$ + SWNA$_S$) is caused by a downward trend in $\overline{P}$. These prior results have been extended here by parsing the effects of $\overline{P}$ and $\overline{E}$ by subregion and season, showing significant spatial and seasonal variations in SWNA aridification that are important to consider when analyzing the impacts of climate change on SWNA hydrology.

SWNA aridification is distinguished from the droughts of the past because it is caused by long-term trends in P and E that are related to anthropogenic global warming rather than the episodic ocean-forced precipitation deficits that characterize historical SWNA drought. Aridification is most pronounced in the cold season surface moisture balance of each subregion, which drops below the range of interannual variability by the end of the 21st century. The downward trend in cold season $\overline{P - E}$ is caused by increasing $\overline{E}$ in ^{C}SWNA$_N$ and by decreasing $\overline{P}$ in ^{C}SWNA$_S$. We think this is related to the poleward expansion of the Hadley circulation that reduces cold season P in ^{C}SWNA$_S$, but not in ^{C}SWNA$_N$. Elevated global temperatures alter the amount of snowpack and timing of snow melt, and cause more cold season P to fall as rain rather than snow, all of which enhances $\overline{E}$ in CMIP5 projections for ^{C}SWNA$_N$. The ENSO and PDO climate variability indices modulate the interannual fluctuations in cold season SWNA P that are superimposed over the century-scale drying trends in CMIP5 projections of 21st century climate.

Downward trends in $\overline{P-E}$ are relatively smaller in magnitude in the warm season and are caused by decreasing $\overline{P}$ in both $^{W}SWNA_{N}$ and $^{W}SWNA_{S}$. Warm season $\overline{P-E}$ remains within the range of interannual variability throughout the 21st century in both subregions, however the drying trend in $\overline{P-E}$ is expected to affect local temperatures, wildfire frequency, and ecological water demands. Together, the warm and cold season projections of SWNA $\overline{P-E}$ foretell a future of sustained drier conditions that will exacerbate water scarcity issues across SWNA over the next century.

Figures

Figure 1. (a) The spatial extent of subregions $SWNA_N$ (117°W to 99°W and 32.5°N to 40°N), $SWNA_S$ (117°W to 99°W and 25°N to 32.5°N), and the entire SWNA ($SWNA_N$ + $SWNA_S$). CMIP5 precipitation (P) and latent heat flux (converted to evaporation, E) values are averaged across all model grid cells that are located completely within or <1° outside of the boundaries of the averaging areas. Grid cells containing less than 80% land surface area are not included in the spatial averages. (b) CMIP5 ocean surface air temperature (T) values are averaged across the North Atlantic (5°N-60°N, 52°W-17°W), the North Pacific (21°N-49°N, 186°W-138°W), and the Tropical Pacific (5°S-5°N, 170°W-120°W) oceans to capture simulated climate variability associated with the Atlantic Multidecadal Oscillation, the Pacific Decadal Oscillation and the El Niño Southern Oscillation.
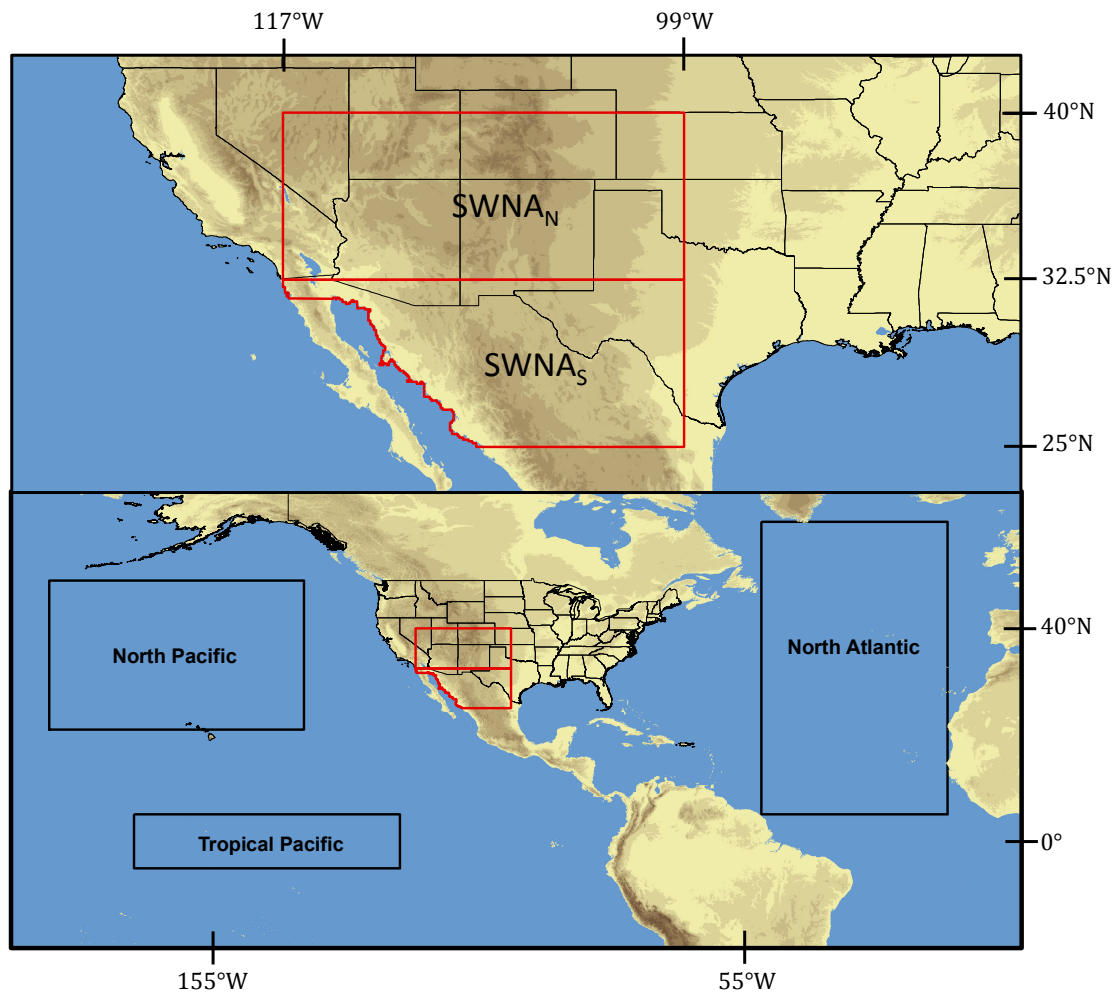
Figure 2. Time series of cold season P (top), E (middle), and $P - E$ (bottom) for $SWNA_N$ are shown in mm/month for each of the 18 CMIP5 models (colored lines) plus the ensemble mean (black lines) to demonstrate the spread of the model output. The Historical (1861-2005) and RCP8.5 (2006-2100) simulations are concatenated to form continuous time series from 1861-2100.

Figure 3. Time series of cold season Tropical Pacific (TPac) Ocean surface air temperatures (T) associated with the El Niño Southern Oscillation (ENSO) are shown in degrees Celsius for each of the 18 CMIP5 models (colored lines) plus the ensemble mean (black line) to demonstrate the spread of the model output. The Historical (1861-2005) and RCP8.5 (2006-2100) simulations are concatenated to fo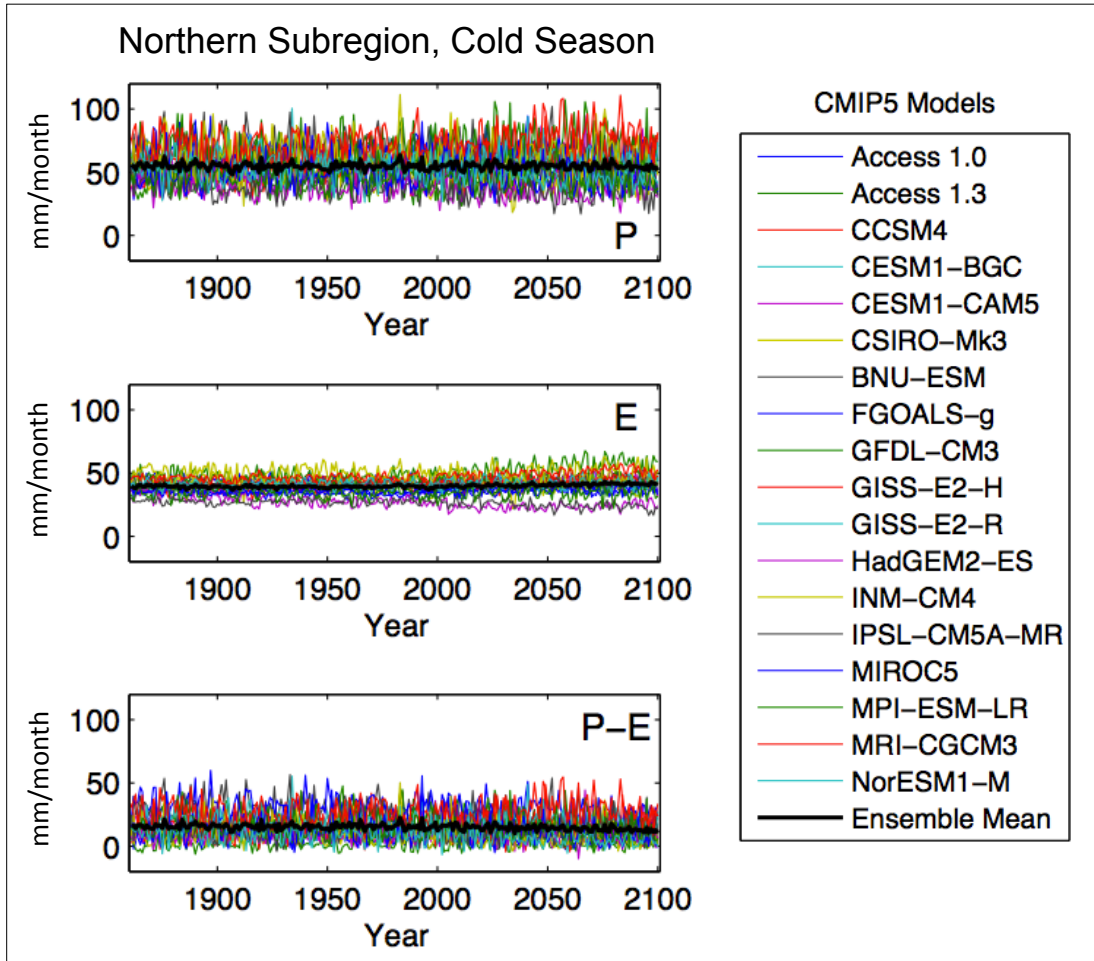rm continuous time series from 1861-2100. TPac T increases in the 21st century once the anthropogenic radiative forcing starts to follow the RCP8.5 pathway beginning in the year 2006.
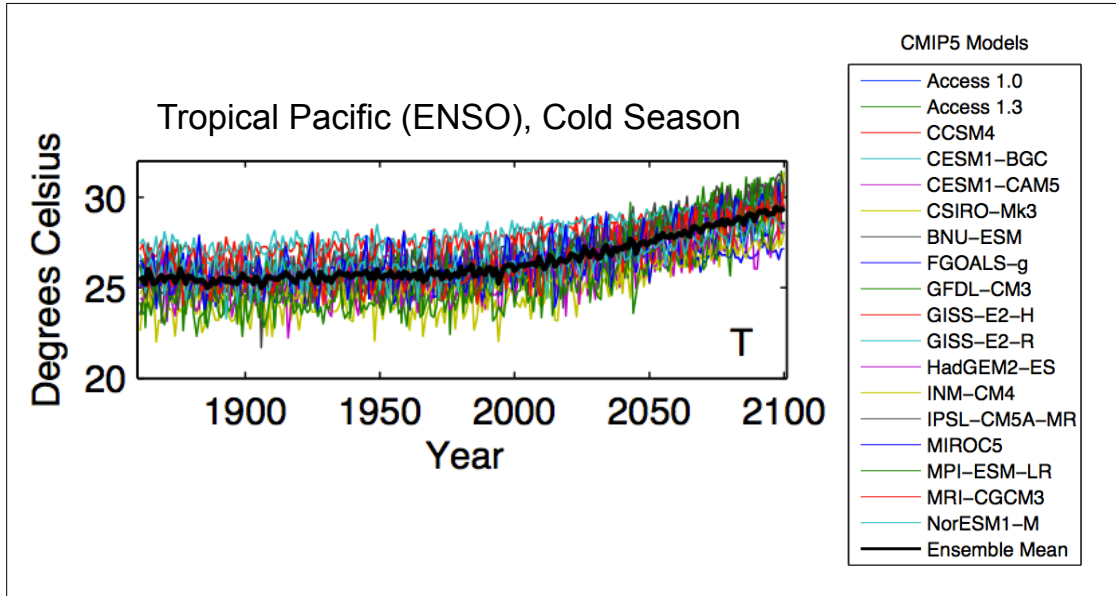
Figure 4. The 18-model ensemble mean anomalies of $\overline{P}$ (blue), $\overline{E}$, (red), and $\overline{P-E}$ (green) (mm/month) are shown for the northern (SWNA$_N$) and southern (SWNA$_S$) subregions of SWNA during the cold (December-May) and warm (June-November) half-yearly seasons (denoted with superscripts ^{C} and ^{W}). $\overline{P}$, $\overline{E}$, and $\overline{P-E}$ are shown relative to their 1861-1960 simulated historical means (y=0). The 25th to 75th percentile range of $P-E$ over the entire 18-model ensemble is shown as a smoothed envelope using a 21-year centered moving average (gray shading). Historical (1861-2005) and RCP8.5 (2006-2100) simulations are concatenated to form continuous time series from 1861-2100. The fraction of total variance in $\overline{P-E}$ that is accounted for by $\overline{P}$ is shown for each subregion and season.
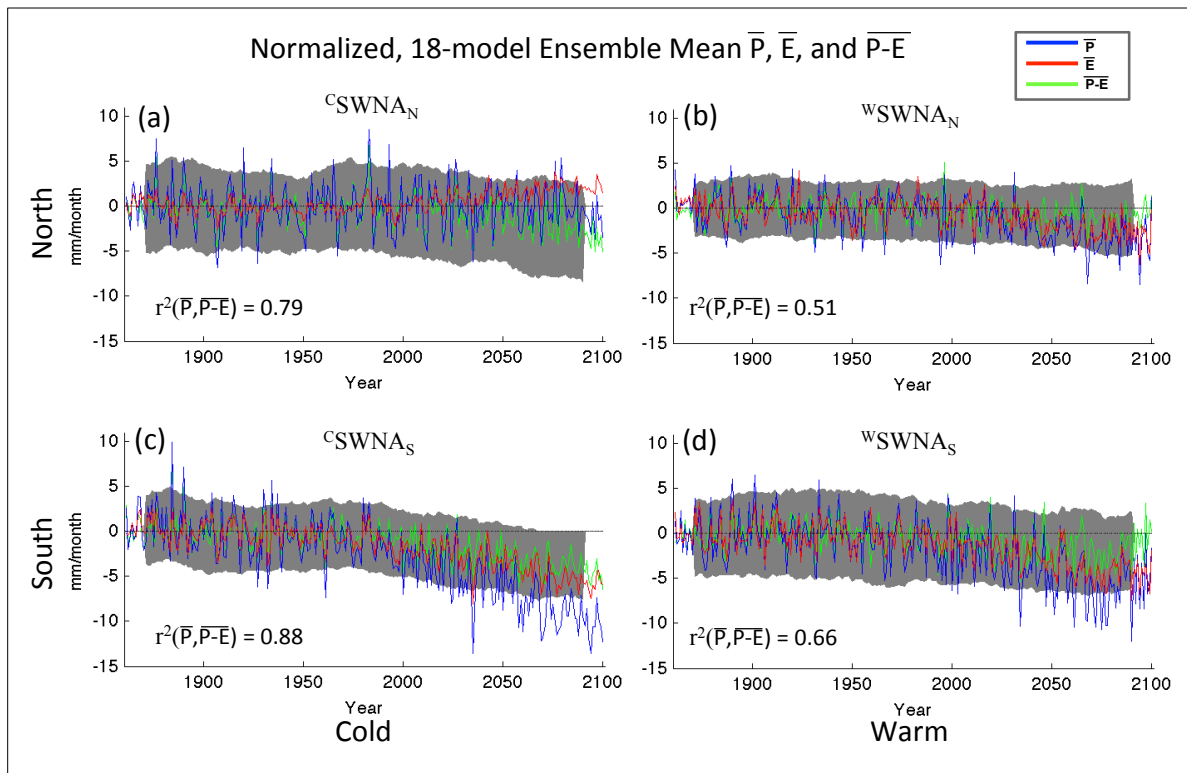
Figure 5. Ensemble mean projected $\overline{P-E}$ (red line, mm/month) is shown for the SWNA$_N$ and SWNA$_S$ subregions during the cold (December-May) and warm (June-November) half-yearly seasons (denoted with superscripts ^{C} and ^{W}). Projected $\overline{P-E}$ is shown relative to the 1861-1960 simulated historical mean (y=0). Detrended time series (blue line) are calculated by removing the 2006-2100 linear trend (black line) from the projected $\overline{P-E}$ time series. The range of interannual variability (blue shading) includes all values between the minimum and maximum values of the detrended time series. The fraction of the variance in the projected $\overline{P-E}$ that is accounted for by the projected trend in $\overline{P-E}$ is shown for each subregion and season.

31
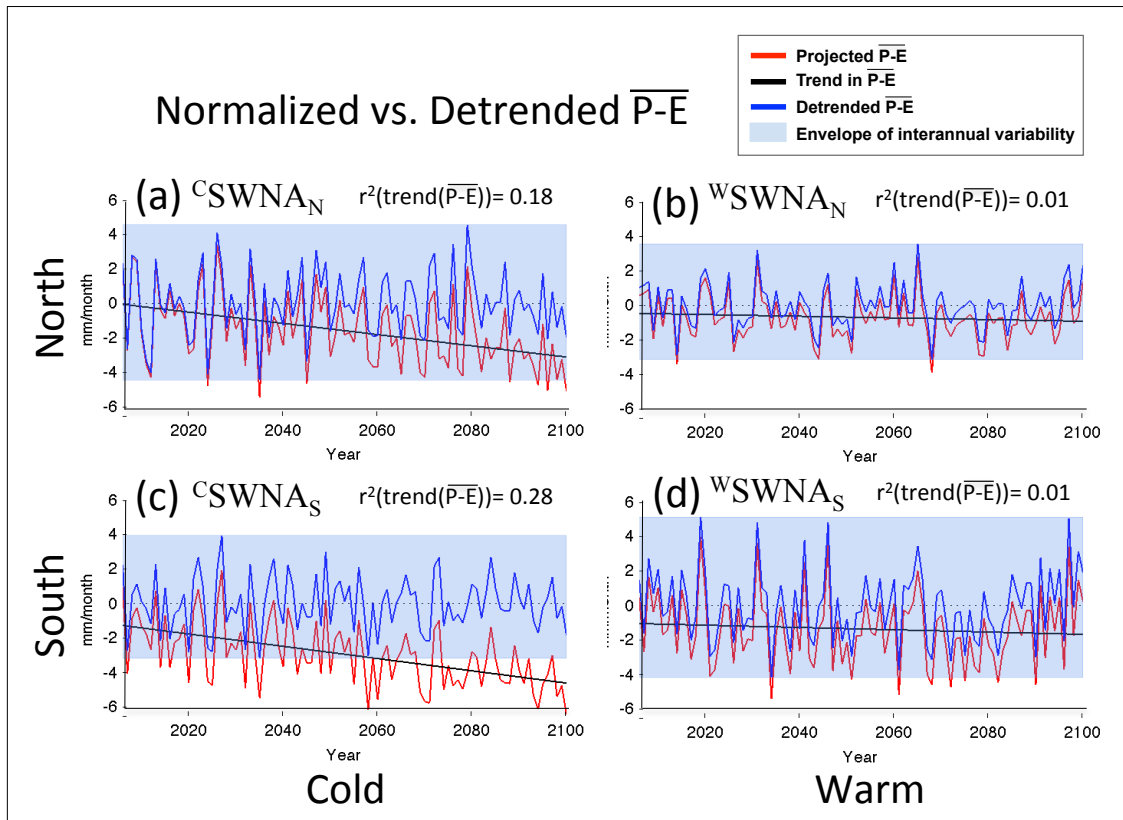
Appendix B

Tables

Table 1. The CMIP5 models used in this analysis are listed along with their spatial resolutions. A single iteration from the Historical and RCP8.5 simulations are analyzed for each of the 18 models in the ensemble.

Model	Modeling Center	Model Resolution
ACCESS1.0	Commonwealth Scientific and Industrial Research Organization; Bureau of Meteorology	1.25°×1.875°
ACCESS1.3	Commonwealth Scientific and Industrial Research Organization; Bureau of Meteorology	1.25°×1.875°
BNU-ESM	College of Global Change and Earth System Science, Beijing Normal University	2.81°×2.81°
CCSM4	National Center for Atmospheric Research	0.94°×1.25°
CESM1-BGC	National Center for Atmospheric Research	0.94°×1.25°
CESM1-CAM5	National Center for Atmospheric Research	0.94°×1.25°
CSIRO-Mk3.6	Commonwealth Scientific and Industrial Research Organization in collaboration with Queensland Climate Change Center of Excellence	1.875°×1.875°
FGOALS-G2.0	Institute of Atmospheric Physics, Chinese Academy of Sciences, Tsinghua University	3°×2.81°
GFDL-CM3	NOAA Geophysical Fluid Dynamics Laboratory	2°×2.5°
GISS-E2-H	NASA Goddard Institute for Space Studies	2°×2.5°
GISS-E2-R	NASA Goddard Institute for Space Studies	2°×2.5°
HadGEM2-ES	Met Office Hadley Center	1.25°×1.875°
INM-CM4	Institute for Numerical Mathematics	1.5°×2°
IPSL-CM5A-MR	Institut Pierre-Simon Laplace	1.26°×2.5°
MIROC5	Atmosphere and Ocean Research Institute, National Institute for Environmental Studies; Japan Agency for Marine-Earth Science and Technology	1.4°×1.4°
MPI-ESM-LR	Max Plank Institute for Meteorology	1.875°×1.875°
MRI-CGCM3	Meteorological Research Institute	1.125°×1.125°
NorESM1-M	Norwegian Climate Centre	1.875°×2.5°

Table 2. Regression coefficients for the 1861-2100 linear trends in the 18-model ensemble mean precipitation ($\overline{P}$), evaporation ($\overline{E}$), and surface moisture balance ($\overline{P-E}$). Model biases were removed by subtracting the 1861-1960 mean from each time series before calculating $\overline{P}$, $\overline{E}$, and $\overline{P-E}$. Linear trends are calculated for the northern (SWNA$_N$), southern (SWNA$_S$), and combined northern and southern regions (SWNA), separately for cold (December-May) and warm (June-November) half yearly seasons (denoted with superscripts ^{C} and ^{W}). The annually averaged linear trend across the entire SWNA (^{A}SWNA) is shown. All trends are statistically significant ($\alpha = 0.05$) except for ^{C}SWNA$_N$ $\overline{P}$ (in parentheses).

Linear Trends (mm·month^{-1}·century^{-1})				
		$\overline{P}$	$\overline{E}$	$\overline{P-E}$
Cold	^{C}SWNA$_N$	(-0.2)	1.0	-1.2
	^{C}SWNA$_S$	-4.7	-2.7	-2.1
	^{C}SWNA	-2.2	-0.7	-1.6
Warm	^{W}SWNA$_N$	-1.8	-1.3	-0.5
	^{W}SWNA$_S$	-3.0	-2.1	-0.9
	^{W}SWNA	-2.3	-1.7	-0.7
Annual	^{A}SWNA	-2.3	-1.2	-1.1

Table 3. The percentage of the 18 CMIP5 simulations that yield significant correlations (α = 0.05) between SWNA precipitation (P) in the northern or southern subregions (denoted SWNA$_N$ and SWNA$_S$) and ocean surface air temperature anomalies (T) over the North Atlantic (NAtl), North Pacific (NPac), and Tropical Pacific (TPac) oceans. Correlations are calculated over the Historical (1861-2005) and RCP8.5 (2006-2100) periods. The percentages of significant correlations are arranged by season, with cold season (December-May) correlations on the left (a and c; denoted with superscript ^{C}) and warm season (June-November) correlations on the right (b and d; denoted with superscript ^{W}). Significant correlations are counted only if r>0 for r(SWNA P, TPac T) or if r<0 for r(SWNA P, NPac T) and r(SWNA P, NAtl T). Cells in which the percentage of significant correlations is >33% are highlighted in blue where r>0 and in orange where r<0.

North

(a) ^{C}SWNA$_N$	Historical	RCP8.5
r(P, ^{C}NAtl T)	0%	0%
r(P, ^{C}NPac T)	61%	67%
r(P, ^{C}TPac T)	94%	89%

(b) ^{W}SWNA$_N$	Historical	RCP8.5
r(P, ^{W}NAtl T)	0%	0%
r(P, ^{W}NPac T)	6%	0%
r(P, ^{W}TPac T)	78%	78%

South

(c) ^{C}SWNA$_S$	Historical	RCP8.5
r(P, ^{C}NAtl T)	6%	6%
r(P, ^{C}NPac T)	39%	11%
r(P, ^{C}TPac T)	89%	61%

(d) ^{W}SWNA$_S$	Historical	RCP8.5
r(P, ^{W}NAtl T)	0%	17%
r(P, ^{W}NPac T)	0%	0%
r(P, ^{W}TPac T)	56%	50%

Cold   Warm

References

Barnett, T. P., and Coauthors, 2008: Human-induced changes in the hydrology of the western United States. *Science*, **319**, 1080–1083, doi:10.1126/science.1152538.

Burke, E. J., Brown, S. J., and Christidis, N., 2006: Modeling the recent evolution of global drought and projections for the twenty-first century with the Hadley Centre climate model. *J. of Hydrometeor.*, **7**, 1113–1125, doi:10.1175/JHM544.1.

Cayan, D. R., Das, T., Pierce, D. W., Barnett, T. P., Tyree, M., and Gershunov, A., 2010: Climate change and water in Southwestern North America special feature: Future dryness in the southwest US and the hydrology of the early 21st century drought. *Proc. Natl. Acad. Sci.*, **107**, 21271–21276, doi:10.1073/pnas.0912391107.

Cook, B. I., and Seager, R., 2013: The response of the North American Monsoon to increased greenhouse gas forcing. *J. Geophys. Res.-Atmos.*, **118**, 1690–1699, doi:10.1002/jgrd.50111.

Douglas, M. W., Maddox, R. A., Howard, K., and Reyes, S., 1993: The Mexican Monsoon. *J. Climate*, **6**, 1665–1677, doi:10.1175/1520-0442(1993)006<1665:TMM>2.0.CO;2.

Gershunov, A., and Barnett, T. P., 1998: Interdecadal modulation of ENSO teleconnections. *Bull. Amer. Meteor. Soc.*, **79**, 2715–2725, doi:10.1175/1520-0477(1998)079<2715:IMOET>2.0.CO;2.

Gutzler, D. S., 2013: Regional climatic considerations for borderlands sustainability. *Ecosphere*, **4(1)**, doi:10.1890/ES12-00283.1.

Gutzler, D. S., Kann, D. M., and Thornbrugh, C., 2002: Modulation of ENSO-based long-lead outlooks of Southwestern US winter precipitation by the Pacific Decadal Oscillation. *Wea. Forecasting*, **17**, 1163–1172, doi:10.1175/1520-0434(2002)017<1163:MOEBLL>2.0.CO;2.

Gutzler, D. S., and Keller, S. J., 2012: Observed trends in snowpack and spring season soil moisture affecting New Mexico. *NM J. Sci.*, **46**, 169–182.

Gutzler, D. S., and Preston, J. W., 1997: Evidence for a relationship between spring snow cover in North America and summer rainfall in New Mexico. *Geophys. Res. Lett.*, **24**, 2207–2210, doi:10.1029/97GL02099.

Gutzler, D. S., and Robbins, T. O., 2010: Climate variability and projected change in the western United States: regional downscaling and drought statistics. *Climate Dyn.,* **37**, 835–849, doi:10.1007/s00382-010-0838-7.

Held, I. M., and Soden, B. J., 2006: Robust responses of the hydrological cycle to global warming. *J. Climate*, **19(21)**, 5686–5699, doi:10.1175/JCLI3990.1.

Hoerling, M., and Eischeid, J., 2007: Past peak water in the Southwest. *Southwest Hydrol*, 6:18 ff. http://www.swhydro.arizona.edu/

Hurd, B. H., and Coonrod, J., 2012: Hydro-economic consequences of climate change in the upper Rio Grande. *Climate Res.,* **53**, 103–118, doi:10.3354/cr01092.

IPCC [Stocker, T.F., D. Qin, G.-K. Plattner, M. Tignor, S.K. Allen, J. Boschung, A. Nauels, Y. Xia, V. Bex and P.M. Midgley], 2013: *Climate Change 2013: The Physical Science Basis. Contribution of Working Group I to the Fifth Assessment Report of the Intergovernmental Panel on Climate Change*. Cambridge University Press, 1535 pp.

Knowles, N., Dettinger, M.D., and Cayan, D. R., 2006: Trends in snowfall versus rainfall in the western United States. *J. Climate*, **19**, 4545–4559, doi:10.1175/JCLI3850.1.

Llewellyn, D. K., S. Vaddey, Roach, J. D., and Pinson, A., 2013: *West-Wide Climate Risk Assessment: Upper Rio Grande Impact Assessment*. U. S. Department of Interior, Bureau of Reclamation, Upper Colorado Region, Albuquerque Area Office, 169 pp.

Mantua, N. J., and Hare, S. R., 2002: The Pacific decadal oscillation. *J. Oceanogr.*, **58**, 35–44, doi:10.1023/A:1015820616384.

McCabe, G. J., Palecki, M. A., Betancourt, J. L., and Fung, I. Y., 2004: Pacific and Atlantic Ocean influences on multidecadal drought frequency in the United States. *Proc. Natl. Acad. Sci.*, **101**, 4136–4141, doi:10.2307/3371575.

Meinshausen, M., and Coauthors, 2011: The RCP greenhouse gas concentrations and their extensions from 1765 to 2300. *Climatic Change*, **109**, 213–241, doi:10.1007/s10584-011-0156-z.

Melillo, J. M., Richmond, T. C., and Yohe, G. W., 2014: *Climate Change Impacts in the United States: The Third National Climate Assessment*. U.S. Global Change Research Program, 841 pp., doi:10.7930/J0Z31WJ2.

Moss, R. H., and Coauthors, 2010: The next generation of scenarios for climate change research and assessment. *Nature*, **463**, 747–756, doi:10.1038/nature08823.

Mote, P. W., 2003: Trends in snow water equivalent in the Pacific Northwest and their climatic causes. *Geophys. Res. Lett.*, **30**, 1601, doi:10.1029/2003GL017258.

National Oceanic and Atmospheric Administration, accessed 2014: 6-Month climatology maps. [Available online at http://www.drought.gov/nadm/content/climatology-6-month]

Ropelewski, C., and Halpert, M., 1986: North American precipitation and temperature patterns associated with the El Niño Southern Oscillation (ENSO). *Mon. Wea. Rev.*, **114**, 2352–2362, doi:10.1175/1520-0493(1986)114<2352:NAPATP>2.0.CO;2.

Schubert, S., and Coauthors, 2009: A U.S. CLIVAR project to assess and compare the responses of global climate models to drought-related SST forcing patterns: Overview and results. *J. Climate*, **22**, 5251–5272, doi:10.1175/2009JCLI3060.1.

Seager, R., and Coauthors, 2007: Model projections of an imminent transition to a more arid climate in Southwestern North America. *Science*, **316**, 1181–1184, doi:10.1126/science.1139601.

Seidel, D. J., Fu, Q., Randel, W. J., and Reichler, T. J., 2008: Widening of the tropical belt in a changing climate. *Nature Geoscience*, **1**, 21–24, doi:10.1038/ngeo.2007.38.

Sheffield, J., Wood, E. F., and Roderick, M. L., 2012: Little change in global drought over the past 60 years. *Nature*, **491**, 435–438, doi:10.1038/nature11575.

Taylor, K. E., Stouffer, R. J., and Meehl, G. A., 2012: An overview of CMIP5 and the experiment design. *Bull. Amer. Meteor. Soc.*, **93**, 485–498, doi:10.1175/BAMS-D-11-00094.1.

Westerling, A. L., Hidalgo, H. G., Cayan, D. R., and Swetnam, T. W., 2006: Warming and earlier spring increase western US forest wildfire activity. *Science*, **313**, 940–943, doi:10.1126/science.1128834.

Williams, A. P., Allen, C. D., Millar, C. I., Swetnam, T. W., Michaelsen, J., Still, C. J., and Leavitt, S. W., 2010: Forest responses to increasing aridity and warmth in the Southwestern United States. *Proc. Natl. Acad. Sci.*, **107**, 21289–21294, doi:10.1073/pnas.0914211107.

Woodhouse, C. A., Meko, D. M., MacDonald, G. M., Stahle, D. W., and Cook, E. R., 2010: Climate change and water in Southwestern North America special feature: A 1,200-year perspective of 21st century drought in Southwestern North America. *Proc. Natl. Acad. Sci.*, **107**, 21283–21288, doi:10.1073/pnas.0911197107.

Yin, J. H., 2005: A consistent poleward shift of the storm tracks in simulations of 21st century climate. *Geophys. Res. Lett.*, **32**, doi:10.1029/2005GL023684.

Zhang, X., Zwiers, F. W., Hegerl, G. C., Lambert, F. H., Gillett, N. P., Solomon, S., … Nozawa, T., 2007: Detection of human influence on twentieth-century precipitation trends. *Nature*, **448**, 461–U4, doi:10.1038/nature06025.